

# Journal of Biomedical Optics

[SPIDigitalLibrary.org/jbo](http://SPIDigitalLibrary.org/jbo)

## **Quantitative evaluation of the kinetics of human enamel simulated caries using photothermal radiometry and modulated luminescence**

Adam Hellen

Andreas Mandelis

Yoav Finer

Bennett T. Amaechi

# Quantitative evaluation of the kinetics of human enamel simulated caries using photothermal radiometry and modulated luminescence

Adam Hellen,<sup>a,b</sup> Andreas Mandelis,<sup>a,c,d</sup> Yoav Finer,<sup>b</sup> and Bennett T. Amaechi<sup>e</sup>

<sup>a</sup>University of Toronto, Center for Advanced Diffusion-Wave Technologies, Department of Mechanical and Industrial Engineering, 5 King's College Road, Toronto, Ontario, M5S 3G8, Canada

<sup>b</sup>University of Toronto, Faculty of Dentistry, 124 Edward Street, Toronto, Ontario, M5G 1G6, Canada

<sup>c</sup>University of Toronto, Institute of Biomaterials and Biomedical Engineering, 164 College Street, Toronto, Ontario, M5S 3G9, Canada

<sup>d</sup>Quantum Dental Technologies, 748 Briar Hill Avenue, Toronto, Ontario, M6B 1L3, Canada

<sup>e</sup>University of Texas Health Science Center at San Antonio, Department of Comprehensive Dentistry, 7703 Floyd Curl Drive, San Antonio, Texas 78229-3900

**Abstract.** Photothermal radiometry and modulated luminescence (PTR-LUM) is an emerging nondestructive methodology applied toward the characterization and quantification of dental caries. We evaluate the efficacy of PTR-LUM *in vitro* to detect, monitor, and quantify human enamel caries. Artificial caries are created in extracted human molars ( $n = 15$ ) using an acidified gel system (pH 4.5) for 10 or 40 days. PTR-LUM frequency scans (1 Hz–1 kHz) are performed before and during demineralization. Transverse microradiography (TMR) analysis, the current gold standard, follows at treatment conclusion to determine the mineral loss and depth of the artificially demineralized lesions. A theoretical model is applied to PTR experimental data to evaluate the changes in optothermophysical properties of demineralized enamel as a function of time. Higher optical scattering coefficients and poorer thermophysical properties are characteristic of the growing demineralized lesions, as verified by TMR, where the generated microporosities of the subsurface lesion confine the thermal-wave centroid. Enhanced optical scattering coefficients of demineralized lesions result in poorer luminescence yield due to scattering of both incident and converted luminescent photons. PTR-LUM sensitivity to changes in tooth mineralization coupled with opto-thermophysical property extraction illustrates the technique's potential for nondestructive quantification of enamel caries. © 2011 Society of Photo-Optical Instrumentation Engineers (SPIE). [DOI: 10.1117/1.3564909]

Keywords: demineralization; enamel caries; quantitative; photothermal radiometry; modulated luminescence.

Paper 10482SSR received Aug. 29, 2010; revised manuscript received Nov. 9, 2010; accepted for publication Dec. 7, 2010; published online Jul. 1, 2011.

## 1 Introduction

Nondestructive, noninvasive detection of incipient dental caries has gained growing interest over the past several decades as evidence has continually emerged that early implementation of preventive therapies, at the expense of invasive reparative intervention, can promote inorganic ion reuptake (remineralization), lesion consolidation, and/or lesion arrest. Techniques capable of quantifying the extent of lesion progression, while at the same time avoiding continual exposure to harmful ionizing radiation, are invaluable in advancing *in vitro*, *in situ*, and *in vivo* clinical caries detection and diagnosis. The current gold standard in caries research to define lesion extent, mineral loss, and depth is transverse microradiography (TMR).<sup>1</sup> However, the requirement of thin sections clearly obviates its clinical applicability and the ability to investigate intact teeth as they would exist in their natural oral environments. This has led to the ongoing development of nondestructive caries detection techniques and instrumentation, such as DIAGNOdent<sup>TM</sup> and quantitative light-induced fluorescence (QLF<sup>TM</sup>), which are principally based

on optical interaction with bacterial porphyrins and enamel, respectively.

Fundamental processes underlying light-tissue interactions involve optical phenomena within the tissue volume. Parameters used to characterize tissue optical properties include the light scattering ( $\mu_s$ ) and absorption coefficients ( $\mu_a$ ), which refer to the average number of absorption and scattering events per unit length of a photon propagating through a medium.<sup>2</sup> Enamel is a composite material with chemical and structural gradients varying as a function of depth.<sup>3</sup> As a result, light propagation in enamel can be described by the same physical processes as in soft biological tissues (i.e., highly scattering turbid media). This makes the process of optical and thermal property extraction both technically challenging and computationally extensive, typically, involving destructive analysis of thin tissue sections. At visible wavelengths (600–700 nm), optical absorption coefficients of enamel are small ( $\mu_a \leq 1 \text{ cm}^{-1}$ ) compared to the much larger scattering coefficients ( $\mu_s = 20 - 60 \text{ cm}^{-1}$ ).<sup>4,5</sup> Historically, optical properties of enamel have been determined by measurements of the reflectance and transmittance through thin sections followed by the application of a theoretical formalism to the experimental data to extract optical absorption

Address all correspondence to Andreas Mandelis, University of Toronto, Department of Mechanical and Industrial Engineering, 5 King's College Road, Toronto, Ontario, M5S 3G8, Canada. Tel: 416-978-5106; Fax: 416-978-5106; E-mail: mandelis@mie.utoronto.ca

and scattering coefficients. An accurate measurement of the optical coefficients means that light distribution and transport processes within a medium can be almost completely characterized. Larger values for the aforementioned optical coefficients indicate that incident photons are rapidly absorbed, resulting in smaller optical penetration depths and poorer resolution of deeper underlying structures. This illustrates a major setback for purely optical-based systems, such as DIAGNOdent and QLF. Because most laser-tissue interactions are thermal in nature, the optical-to-thermal energy conversion reactions following photon absorption and the subsequent nonradiative heat conversion, propagation/decay, and tissue responses are important physical parameters to consider. Thermal parameters include thermal diffusivity ( $\alpha$ ) and thermal conductivity ( $\kappa$ ), which refer to the rate and amount of heat diffusion through a medium, respectively. Thermal diffusivity ( $\alpha$ ) is an important thermophysical parameter given by the following equation:  $\alpha = \kappa/\rho C$ , where  $\kappa$  is the thermal conductivity,  $\rho$  is the density, and  $C$  is the specific heat. Thermal diffusivity of enamel is approximately  $4.20\text{--}4.69 \times 10^{-7} \text{ m}^2\text{s}^{-1}$ ,<sup>6,7</sup> and conductivity about  $0.87\text{--}0.93 \text{ Wm}^{-1}\text{K}^{-1}$ .<sup>7,8</sup> Independent measurements of optical and thermal properties of carious enamel are scarce, mainly due to the technical challenges and difficulties in preparing thin sections from demineralized tooth specimens. The accuracy and reliability of previously published values of thermal diffusivity was questioned by Panas et al.,<sup>9</sup> citing that significant sample preparation adds additional sources of variability, exacerbating intra- and intersample biological differences. This emphasizes the importance of developing noninvasive, nondestructive methodologies in dental caries research, using quantitative enamel and/or dentin optical and thermophysical properties.

As a dental nondestructive technique, frequency-domain photothermal radiometry (PTR) is an emerging sensitive methodology to characterize pathological dental tissues.<sup>10–13</sup> PTR is based on the generation of diffuse-photon-density waves within a medium, stimulated by irradiation with a harmonically modulated laser beam to induce an oscillatory temperature thermal-wave field, which is captured by mid-IR detectors. The amplitude of the photothermal signal refers to the overall signal magnitude at a given frequency, whereas the phase represents the delay in the photothermal signal collected by the IR detector with respect to a reference signal. The photothermal methodology can be simplified, through normalization, by first considering a homogeneous substrate, for instance, a uniform metal. In metals, optical absorption depths are restricted to the nanometer scale. This results in heat generation at the surface of the metal, which diffuses, via conductive heat transfer, into the bulk material to depths far greater than the optical absorption depth. The deeper penetration of the thermal field compared to the purely optical field underscores the sensitivity of photothermal techniques to the inspection of optically opaque or scattering materials well beyond the range of optical imaging devices. The depth penetration of the thermal-wave field, and thus, the overall depth resolution of the photothermal technique, is governed by the thermal diffusion length,  $\mu = \sqrt{2\alpha/\omega}$ , which heavily relies on the thermal properties of the sample ( $\alpha$ , thermal diffusivity) and the laser beam angular modulation frequency ( $\omega$ ). Thus, a material of high thermal diffusivity or stimulated under low modulation frequency will enhance propagation and capture of thermal waves deeper into the medium.

In nonmetallic polycrystalline materials, such as teeth, the case is much different. Longer optical absorption depths mean that absorption processes are not limited to the surface and, as a result, photothermal effects cannot be considered as a simple surface heat source. As optical absorption and scattering (extinction) depths are longer, elemental heat sources can arise within the bulk of the medium, resulting in an oscillatory temperature field (thermal waves) beyond the thermal diffusion length, over the sample optical extinction length. The concomitant temperature rise results in the generation of thermal infrared photons that can propagate outward to the surrounding medium by virtue of IR spectral transparencies (“windows”) of the enamel and be captured by suitable IR detectors. The resultant thermophotonic PTR signal in nonopaque solids is derived from optical absorption and photothermal-wave generation, which creates a modulation in the temperature of the sample down to a thermal diffusion length (or extinction length, whichever is longer) and integrates all contributions over the depth of the sample.<sup>14,15</sup>

As a complementary signal channel to PTR, modulated luminescence (LUM) monitors the optical-to-radiative energy conversion, where photon absorption and excitation to a higher energy state is followed by de-excitation to a lower energy state and emission of longer wavelength photons. As a purely optical technique, the higher scattering coefficients of enamel and dentin significantly limit optical penetration depths. However, LUM can be very useful as an energy-conversion pathway complementary to PTR, thereby assisting interpretation of signals in the form of physical processes involving optical and thermal parameters of enamel.

The combination of PTR and LUM amplitude and phase signals provides four sensitive channels to indirectly assess the physical condition and the state of health of teeth. Earlier PTR-LUM studies *in vitro* have demonstrated the ability to detect and longitudinally monitor simulated proximal lesions,<sup>12</sup> pit and fissure caries,<sup>10</sup> and artificial demineralized and remineralized carious lesions on root dentin and enamel of human teeth.<sup>13</sup> Thanks to the development of PTR to detect thermal waves along with its rigorous, comprehensive theoretical underpinnings describing the generated thermal signal inside a sample, the nondestructive extraction of optical and thermophysical material properties from enamel has been made possible. Earlier reports on frequency-domain PTR measurements introduced a robust and complex fitting algorithm for the generation of independent sets and simultaneous extraction of optical and thermal parameters and thickness values for each effective layer considered in the three-layer tissue model analysis.<sup>16,17</sup> The computational algorithm was further advanced by Hellen et al.<sup>18</sup> and proved to be a robust and effective model for the nondestructive quantification of lesion thicknesses and the reconstruction of optothermophysical depth profiles of evolving enamel demineralization.

The aim of the present study was to evaluate the ability and efficacy of PTR-LUM to detect, longitudinally monitor and quantify artificial enamel demineralized lesions, simulating initial carious lesions. The objectives were to identify a relationship between PTR-LUM amplitude and phase signals to histological features of demineralized lesions through microradiographic analysis and to apply a coupled diffuse-photon-density and thermal wave model for the extraction of optothermophysical

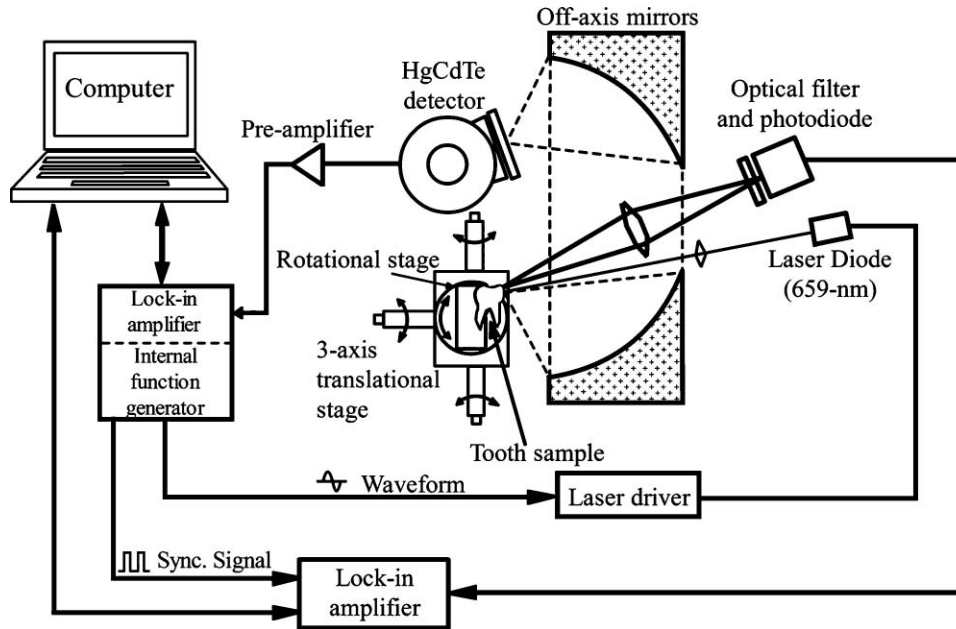


Fig. 1 Schematic of the PTR-LUM experimental setup.

properties from PTR signals in order to relate these changes in properties to morphological changes during demineralization. Overall, this study is important in establishing PTR-LUM as a sensitive analytical technique for the nondestructive evaluation of mineralized multilayered enamel and for the quantitative characterization of the fundamental processes governing enamel demineralization.

## 2 Materials and Methods

### 2.1 Production of Smooth-Surface Enamel Artificial Caries

Fifteen sound human molars extracted for orthodontic or other surgical purposes were collected, debrided of all soft tissue, and sterilized using  $\gamma$  irradiation (4080 Gy) prior to use. The study protocol was approved by the University of Toronto Ethics Review Board (Protocol No. 25075). Individual samples were mounted on LEGO® blocks to allow for the precise realignment of samples on the micrometer-scale three-axis precision stage during subsequent measurements. An acid-resistant nail varnish was applied to all surfaces of the teeth except a delimited 6×6 mm lingual/palatal enamel treatment window, which was exposed to the artificial demineralizing medium and probed with the PTR-LUM system. Artificial smooth-surface enamel demineralization simulating initial carious lesions were induced using a well-characterized acidified gel system.<sup>19,20</sup> The demineralizing gel contained 0.1 M lactic acid gelled to a thick consistency with 6% (w/v) hydroxyethyl cellulose (HEC) and adjusted to pH 4.5 by the addition of 0.1 M NaOH.<sup>21</sup> Samples were individually exposed to 30 mL of the demineralizing medium for 10 ( $n = 10$ ) or 40 days ( $n = 5$ ) in order to investigate incipient and more advanced lesions. During the 40-day exposure period, fresh aliquots of the gel medium were replaced after 20 days. All measurements were performed at room temperature and constant humidity in a laboratory-controlled environment.

### 2.2 Photothermal Radiometry and Modulated Luminescence Experimental Setup and Measurements

The PTR-LUM experimental setup is shown in Fig. 1. The laser light source was a semiconductor laser diode emitting at 659 nm (Mitsubishi ML101J27, Thorlabs, Newark, New Jersey; optical power output = 130 mW, beam size  $\approx$  5.60 mm). A diode laser driver (LDC 210, Thorlabs, Newark, New Jersey) triggered by the built-in function generator of the lock-in amplifier (SR830, Stanford Research Systems, Sunnyvale, California) modulated the laser current harmonically. The modulated infrared PTR signal from the tooth was collected and focused by two off-axis paraboloidal mirrors (Melles Griot 02POA017, Rhodium coated, Albuquerque, New Mexico) onto a mercury cadmium telluride (MCT) detector (Judson Technologies J15D12, Montgomeryville, Pennsylvania; spectral range: 2–12  $\mu$ m, peak detectivity  $\approx$   $5 \times 10^{10}$  cm Hz<sup>1/2</sup> W<sup>-1</sup> at ca. 12  $\mu$ m) operating at cryogenic temperatures by means of a liquid-nitrogen cooling mechanism and with an active area of 1 mm<sup>2</sup>. Before being sent to the lock-in amplifier, the PTR signal was amplified by a preamplifier (Judson Technologies PA-101, Montgomeryville, Pennsylvania). The collected modulated luminescence was focused onto a silicon photodiode with a colored glass filter (Oriel 51345, cut-on wavelength: 715 nm) placed in front of the photodetector to block laser light reflected or scattered by the tooth. For monitoring the modulated luminescence signal, a second lock-in amplifier (SR850, Stanford Research Systems, Sunnyvale, California) was used. Both lock-in amplifiers were controlled by a computer via USB to RS-232 port connections.

Data were collected from each sample by a single point measurement with a laser beam size of 5.6 mm. The incident laser beam was oriented normal to the sample surface. The expanded laser beam was implemented for the theoretical analysis to ensure one-dimensional heat propagation within the sample [i.e., contributions to the overall data from lateral heat diffusion that

is captured by the infrared detector (with 1-mm<sup>2</sup> active area) are negligible].

Frequency scans measured PTR and LUM signals during a scan of laser beam modulation frequency from 1 Hz to 1 kHz in the center of the delineated treatment window before and periodically during the acid treatment. The frequency range was segmented into 21 steps on a logarithmic scale by Labview-controlled computer software (National Instruments, Austin, Texas) to automatically increment frequencies sequentially. Twenty-four seconds of stabilization time were implemented following a change in frequency before data were recorded, amounting to a complete frequency scan time of 20 min. For the 10-day treated samples, PTR-LUM measurements were performed after 5 and 10 days and for the 40-day treated samples, PTR-LUM measurements were carried out on day 5, 10, 15, 20, 30, and 40. Standardized measurement conditions were implemented for all sample frequency scans during the course of treatment. Following each demineralizing treatment, samples were rinsed under running distilled water for 2 min to remove any residual adsorbed gel on the enamel surface. Samples were then dried in ambient air for 1 h and incubated in a sealed chamber containing Petri dishes of distilled water to maintain ambient humidity conditions. Prior to PTR-LUM measurements, samples were removed from the humid chamber, air dried for 20 mins, followed by a further 10 min with the sample placed under direct laser incidence for thermal stabilization. This standardized procedure was followed for all PTR-LUM scans and based on the earlier observation that changes in optical properties, observed as changes in fluorescence intensity, and thermal properties, were negligible following 20 min of stabilization time, for experimentation lasting <1 h.<sup>4,10,22,23</sup> The total drying time implemented in the present study was in line with previous *in vitro* reports employing a 30-min<sup>24</sup> to 45-min<sup>25</sup> stabilizing period.

To obtain meaningful information from PTR frequency-scan data and remove any influence of instrumental effects, the experimentally measured signals were normalized (i.e., they were calibrated against an opaque semi-infinite Glassy Carbon reference sample, as detailed in Hellen et al.<sup>18</sup>).

### 2.3 Transverse Microradiography and Image Analysis

Following completion of all PTR-LUM measurements all samples were subjected to TMR analysis to determine the mineral loss and depth of the artificially demineralized lesions. The samples were sectioned using a water-cooled diamond-coated wire saw model 3242 (Well, Le Locle, Switzerland), to produce a thin enamel slice ~100  $\mu\text{m}$  in thickness. The slice, together with an aluminum step wedge (10 steps of 24.5- $\mu\text{m}$  thickness), was microradiographed on type 1A high-resolution glass X-ray plates (IMTECH, California) with a Phillips x-ray generator system equipped with a nickel filtered Cu-K $\alpha$  target, producing monochromatic radiation of wavelength appropriate for hydroxyapatite (184  $\text{\AA}$ ). The plates were exposed for 10 min at 20 kV/10 mA, and processed. Processing consists of a 5-min development in a developer (Kodak HR) and 15-min fixation in a Rapid-fixer (Kodak) before a final 30-min wash period in distilled water. After drying, the microradiographs were visualized using an optical microscope (Leica DMR, Microsys-

tems, Wetzlar, Germany) linked via a CCTV camera (Sony, XC-75CE) to a personal computer. The enhanced image of the microradiograph was analyzed under standard conditions of light intensity and magnification and processed, along with data from the image of the step wedge, using the TMR software (TMRW version 2.0.27.2, Inspektor Research Inc., Amsterdam, Netherlands)<sup>26</sup> to quantify the lesion parameters of integrated mineral loss (vol. %  $\mu\text{m}$ ) and lesion depth (in microns). The implementation of the latest dedicated TMR software package utilized a new algorithm developed to mathematically flatten curved tooth surfaces, by completing several scans for each microradiographed section. The mineral loss was computed as the difference in volume percent of mineral between sound and demineralized tissue integrated over the lesion depth. The mineral content plateau in deeper regions of the enamel section, representative of sound tissue, was preset at the 87-vol. % level.<sup>26</sup> The lesion depth was determined as the distance from the measured sound enamel surface to the location in the lesion, where mineral content was 95% of the sound enamel mineral volume. Lesion parameters were determined by averaging several scans over the distance of the thin section taken from the center of the treated area and corresponding to the irradiated beam size in PTR-LUM experimental measurements.

### 2.4 Theoretical Model and Multiparameter Fitting of Experimental Curves

Experimental PTR amplitude and phase signals were fitted to the three-layer coupled diffuse-photon-density-wave and thermal-wave theoretical model using the simplex downhill algorithm<sup>27</sup> initially applied by Matvienko et al.<sup>17,28</sup> and further advanced by Hellen et al.<sup>18</sup> for the investigation of multilayered sound and demineralized enamel. A detailed description of the theoretical model and the multiparameter fitting procedure used in the present study can be found in Hellen et al.<sup>18</sup> Briefly, the model is based on the computational simulation of optical and thermal fluxes within each effective enamel layer considered in the analysis. The designation of effective layers was based on the sample treatments, where a two- and three-layer approximation was assumed for sound and demineralized enamel, respectively (Fig. 2) and was borne out by TMR cross-sectional images (Figs. 3 and 4). For untreated, intact teeth, the two-layer representation assumed a thin surface layer of finite thickness ( $L_1$ ), where mineral content and optothermal properties vary from underlying semi-infinite sound enamel ( $L_2$ ) and was referred to as “aprismatic” enamel.<sup>29-31</sup> Following the first exposure to the demineralizing agent, the two-layer approximation was no longer valid and, in its place, a three-layer profile was considered, where layer 1 denoted the intact surface layer overlying the demineralized lesion body ( $L_2$ ), followed by semi-infinite sound enamel. The exclusion of dentin in the theoretical representation of intact teeth was justified in terms of its relatively large depth compared to the longest thermal diffusion length (at the lowest modulation frequency) by Hellen et al.<sup>18</sup> The fitting of the experimental PTR data to the theoretical model results in the extraction of multiple optothermophysical parameters for each effective layer. A select subset of all the parameters extracted from the theoretical multiparameter fits of sound and demineralized samples was found to be more reliable and changed more consistently with treatment time.<sup>18</sup> The subset includes the main optical and

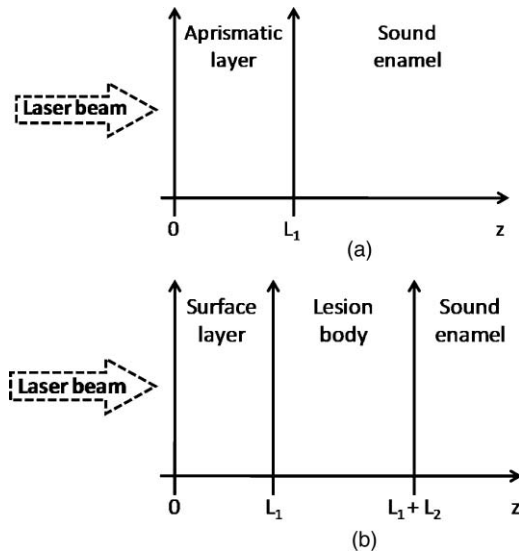


**Fig. 2** Theoretical reconstruction of the effective layers used for the computational fits of (a) sound and (b) demineralized enamel. In the sound enamel approximation,  $L_1$  = aprismatic layer and  $L_2$  = sound enamel. In acid treated enamel,  $L_1$  = surface layer;  $L_2$  = lesion body and  $L_3$  = semi-infinite sound enamel.

thermal transport properties, including optical scattering and absorption coefficients, thermal conductivity and diffusivity, and layer thicknesses. They play a central role in the theory of dental PTR in terms of high signal sensitivity to their variation and form the basis of the present investigation.

Experimental PTR frequency-scan data were fitted across the frequency range of 4–354 Hz. The parameter measurement strategy involved fitting experimental PTR amplitude and phase from untreated sound enamel to the two-layer approximation using parameter limits based on maximum and minimum values defined in the literature.<sup>18</sup> The layer 2 (substrate) parameters generated from the sound enamel fit were then fixed as the properties of the semi-infinite layer 3 in the subsequent three-layer

approximation of demineralized enamel. The final PTR amplitude and phase data after all acid treatments were then fitted using layer thicknesses obtained from TMR mineral content profiles, by defining a minimum and maximum thickness of the surface layer ( $L_1$ ) and lesion body ( $L_2$ ) as described in detail in Hellen et al.<sup>18</sup> The theoretically derived thicknesses thus derived from the final PTR curves were then fixed as the upper limits in order to fit intermediate PTR amplitude and phase curves. The major physically reasonable assumption in the theoretical fitting procedure was that intermediate thicknesses could not be larger than the final thicknesses calculated from the fitting of final PTR signals, which were based on TMR microradiographs.

### 3 Results

#### 3.1 Microradiographic Analysis and Photothermal Radiometry and Modulated Luminescence Signals

Artificial carious lesions were created with an average mineral loss and lesion depth of  $1247 \pm 502$  vol.%  $\mu\text{m}$  and  $90 \pm 12$   $\mu\text{m}$ , respectively, determined from TMR measurements. After 40 days of demineralization, average mineral loss and lesion depth determined from TMR analysis, were  $1468 \pm 592$  vol.%  $\mu\text{m}$  and  $103 \pm 10$   $\mu\text{m}$ , respectively. Representative demineralized lesions treated for 10 and 40 days are shown in Figs. 3 and 4, respectively. Microradiographs confirmed the presence of carious lesions characterized by a distinct lesion body underlying a superficial intact enamel surface layer with mineral volume near, but lower than, the sound enamel level.

PTR-LUM frequency responses for the 10- and 40-day treated samples are also shown in Figs. 3 and 4, respectively. PTR behavior in response to subsurface lesion formation exhibited increases in amplitude across the entire modulation frequency range. In the 10-day treated sample (Fig. 3), a large PTR amplitude increase after five days resulted in slope changes in the frequency response and the onset of curvature predominately at high modulation frequencies, as expected from the depth-profilometric character of this technique (high modulation

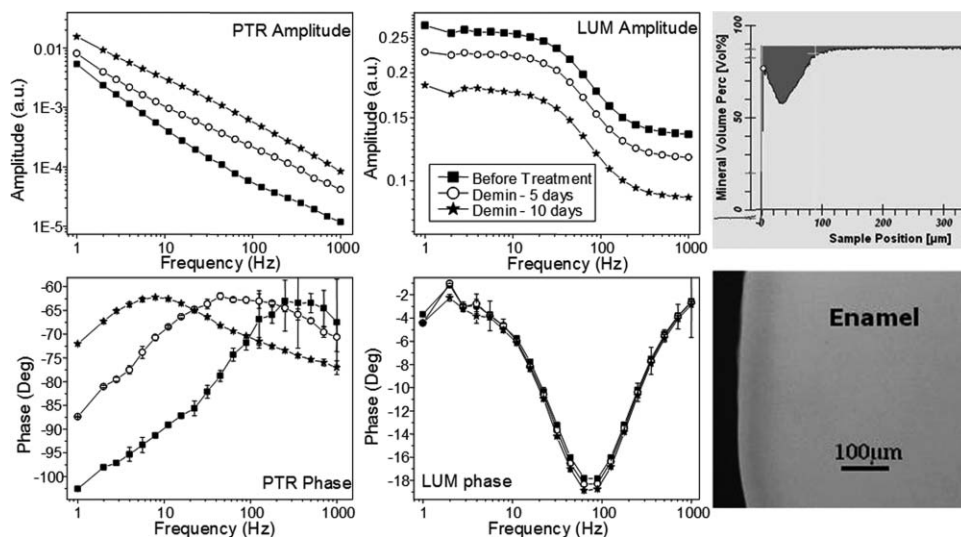


**Fig. 3** PTR-LUM amplitude and phase curves for a representative 10-day demineralized sample. Error bars, when not visible, are of the size of the symbols. The densitometric tracing (top right) and microradiographic image (bottom right) of the lesion are presented in the adjacent figures. From TMR analyses: mineral loss = 1310 vol.%  $\mu\text{m}$ ; surface layer thickness = 3.6  $\mu\text{m}$  and lesion width = 85.0  $\mu\text{m}$ .

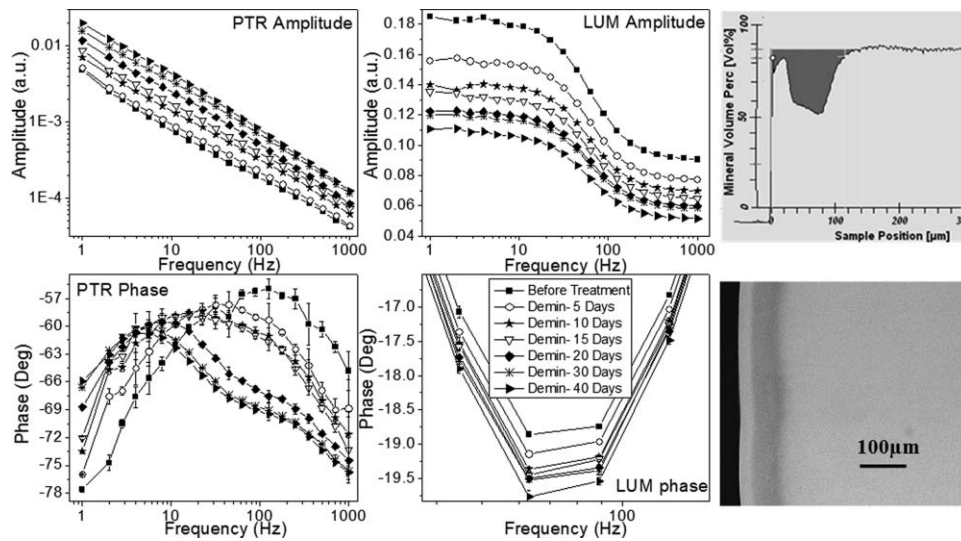


**Fig. 4** PTR-LUM amplitude and phase curves for a representative 40-day demineralized sample. Error bars, when not visible, are the size of the symbols. The densitometric tracing (top right) and microradiographic image (bottom right) of the lesion are presented in the adjacent figures. From TMR analyses: mineral loss = 1420 vol. %  $\mu\text{m}$ ; surface layer thickness = 2.6  $\mu\text{m}$  and lesion width = 112.2  $\mu\text{m}$ .

frequencies correspond to short thermal diffusion lengths). As demineralization progressed, the PTR amplitude increased in a monotonic fashion and the amplitude curvature shifted to lower modulation frequencies. The PTR phase exhibited the highest sensitivity of all PTR and LUM signal channels to demineralization. A clear phase shift of the demineralized curves to lower frequencies with respect to the healthy curve occurred as treatment progressed. The presence of a phase maximum resulted in an increase in phase lag at high frequencies and a decrease at lower frequencies. Similar PTR trends were also observed for the 40-day treated sample (Fig. 4). After 10 days of treatment, PTR amplitude at high modulation frequencies did not change much until the end of treatment, whereas an increase and pronounced curvature were marked at lower modulation frequencies. A phase maximum shift to lower modulation frequencies was also clearly evident over the duration of treatment. Interestingly, after 20 days of acid exposure, a secondary phase hump (shoulder) became apparent at frequencies larger than about 100 Hz.

In the short- (Fig. 3) and long-term (Fig. 4) demineralized samples, the LUM signal channel exhibited consistent trends with treatment time. A monotonic depression in both amplitude and a decrease in phase minima were evident. It is important to note the anticorrelation in the PTR and LUM signals during demineralization, where the largest PTR signal increase corresponded to the largest LUM signal decrease.

### 3.2 Theoretical Analysis of Demineralized Enamel

Optothermophysical parameters were extracted from the theoretical-computational model for sound enamel, 10-day [Figs. 5 and 6(a)] and 40-day [Figs. 6(b) and 7] demineralized samples and plotted as a function of treatment time. The mean values of the extracted optothermophysical parameters from sound versus demineralized enamel are shown in Table 1. Over the 10-day demineralization period, absorption [Fig. 5(a)] and scattering coefficients [Fig. 5(b)] increased in the surface layer (layer 1). Within the lesion body (layer 2), little change

(increase) in the absorption coefficient was found, whereas the scattering coefficient increased linearly from the onset until the end of the 10-day period. Thermophysical properties of both layers, conductivity [Fig. 5(c)] and diffusivity [Fig. 5(d)], became poorer with demineralization, excluding the thermal conductivity of the surface layer, which increased on or before day 10. The resemblance of the layer 2 diffusivity trends [Fig. 5(d)] to those of conductivity [Fig. 5(c)] is indicative that conductivity changes largely control the behavior of diffusivity.

**Table 1** Mean ( $\pm$  S.D.) values of the optothermophysical parameters extracted from the computational analysis of sound enamel and demineralized enamel after the 10-day treatment period ( $n = 10$ ).

Physical parameters	Sound enamel	Demineralized enamel
	Mean $\pm$ S.D.	Mean $\pm$ S.D.
$\mu_{a1}; [\text{m}^{-1}]$	$66 \pm 19$	$88 \pm 39$
$\mu_{a2}; [\text{m}^{-1}]$	$41 \pm 22$	$48 \pm 38$
$\mu_{s1}; [\text{m}^{-1}]$	$771 \pm 1110$	$58496 \pm 61162$
$\mu_{s2}; [\text{m}^{-1}]$	$4947 \pm 1310$	$112604 \pm 30202$
$\alpha_1; [\text{m}^2/\text{s}]$	$5.1 \times 10^{-7} \pm 1.6 \times 10^{-7}$	$6.5 \times 10^{-7} \pm 1.0 \times 10^{-7}$
$\alpha_2; [\text{m}^2/\text{s}]$	$4.4 \times 10^{-7} \pm 1.4 \times 10^{-8}$	$2.8 \times 10^{-7} \pm 5.9 \times 10^{-8}$
$\kappa_1; [\text{W}/\text{mk}]$	$0.44 \pm 0.20$	$0.55 \pm 0.23$
$\kappa_2; [\text{W}/\text{mk}]$	$0.87 \pm 0.05$	$0.46 \pm 0.16$
$L_1; [\mu\text{m}]$	$13.9 \pm 5.6$	$13.2 \pm 4.0$
$L_2; [\mu\text{m}]$	--	$83.6 \pm 21.9$

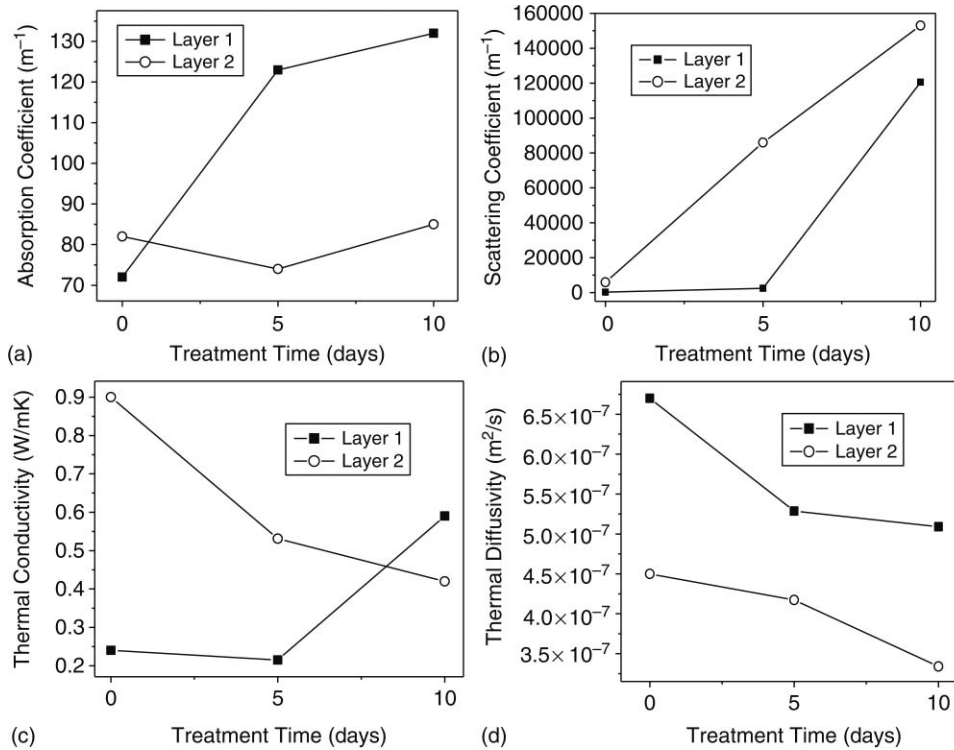


**Fig. 5** The change in (a) optical absorption and (b) scattering coefficients, and (c) thermal conductivity and (d) diffusivity parameters as a function of time over the 10-day demineralization period. Layer 1 = surface layer; layer 2 = lesion body.

Changes in layer thicknesses of the 10- and 40-day demineralized samples are shown in Fig. 6. Over the 10-day period, the thickness, or depth, of the growing subsurface lesion increased nearly linearly [Fig. 6(a)]. At later treatment times [Fig. 6(b)], the depth of layer 2 continued to increase at a lower rate until the end of the 40-day treatment period. With respect to layer 1, slight changes with opposite trends were observed in the two presented samples. The thickness of the surface layer decreased from 0 days over the 10-day period, whereas in the 40-day demineralized lesion, the thickness was stable for the first 15 days followed by a mild increase until the end of the treatment period. The final thicknesses of layers 1 and 2 determined theoretically for the 10-day sample were 6.6 and 81.2  $\mu m$ , respectively, whereas the corresponding theoretically

derived final thicknesses for the 40-day sample were 18.7 and 92.1  $\mu m$ , respectively. Demineralization kinetics of the 40-day demineralized sample is shown in Fig. 8, where the least-squares line fitted to the total lesion depth data, lesion width plus surface layer thickness, revealed a linear relationship as a function of the cube root of time in days. The least-squares line fitted to the data is  $y = 8.80 + 29.13X$ , where the slope is  $29.13 \mu m/t^{1/3}$ , which indicates a subdiffusive progression of enamel demineralization.

Optical and thermophysical properties plotted as a function of time for the 40-day demineralized sample are shown in Figs. 7(a)–7(d). As in the 10-day demineralized sample, the absorption [Fig. 7(a)] coefficients of layers 1 and 2, increased modestly overall over the demineralization period. The scattering coefficients of both surface and subsurface layers, however,

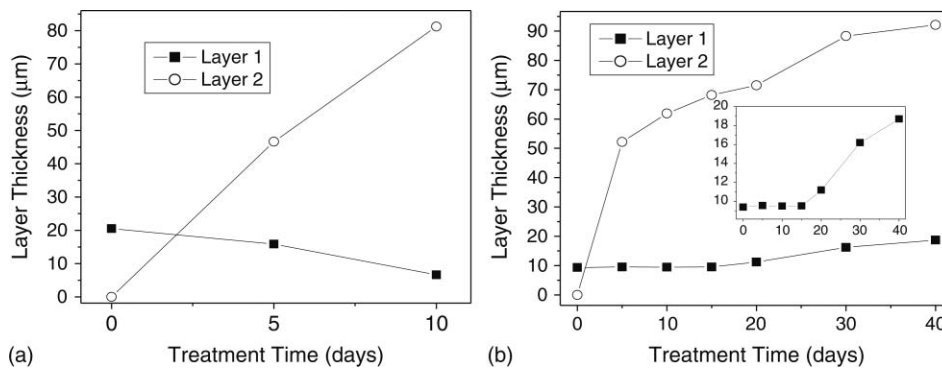


**Fig. 6** Change in layer thicknesses as a function of time for the (a) 10-day and (b) 40-day demineralized samples. Thicknesses of layer 1 at day 0 represent the aprismatic layer in sound enamel. The inset in (b) shows the details of layer 1 thickness over time on an expanded scale. Layer 1 = surface layer; layer 2 = lesion body.

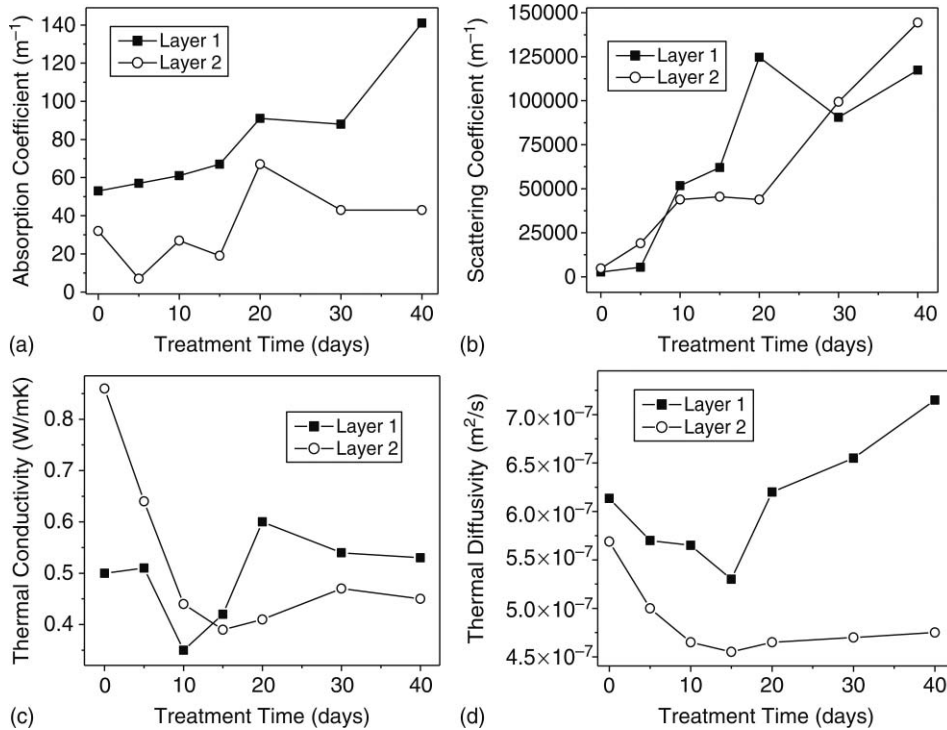


**Fig. 7** The change in (a) optical absorption and (b) scattering coefficients, and (c) thermal conductivity and (d) diffusivity parameters as a function of time over the 40-day demineralization period. Layer 1 = surface layer; layer 2 = lesion body.

increased dramatically over the demineralization time [Fig. 7(b)]. Thermal conductivity [Fig. 7(c)] and diffusivity [Fig. 7(d)] of layer 2 decreased rapidly for the first 10 days of demineralization in a manner similar to the 10-day demineralized sample [Figs. 7(c) and 7(d)], reaching a minimum at 15 days, after which properties slightly increased and stabilized for the remainder of the treatment period. Thermal conductivity and diffusivity of layer 1 behaved similarly; a decrease over the first 15 days was followed by an increase above the baseline level at day 0.

Thermal diffusivity after 20 days increased nearly linearly until the end of treatment. Again, the trends in thermal conductivity appear to largely control the thermal diffusivity behaviour in this sample.

## 4 Discussion

During demineralization consistent trends of increasing PTR amplitude with a concomitant decrease in PTR phase lag and a shift of the phase peaks to lower frequencies were observed (Figs. 3 and 4). These trends suggest the formation of a depthwise growing subsurface lesion as has been documented elsewhere.<sup>11,13,32</sup> Changes in PTR phase with demineralization are attributed to thermal-wave interference patterns within the demineralized lesion, which increases in thickness during the demineralization period.<sup>33</sup>

### 4.1 Multiparameter Fits of Photothermal Radiometry Experimental Data during Demineralization

PTR amplitude and phase trends can be explained based on the generated set of optical and thermal properties of each effective layer (Figs. 5–7). Theoretical approximations of carious lesions are often restricted to two layers, where the surface layer is neglected because its thickness is typically small compared to the thickness of the demineralized lesion.<sup>34</sup> However, preliminary attempts to fit the present PTR data to a two-layer approximation yielded a very poor fit of the experimental and theoretical curves. This can be attributed to the significant contribution from the intact surface layer to the exponentially decreasing thermal-wave depth profile, which was significant enough so

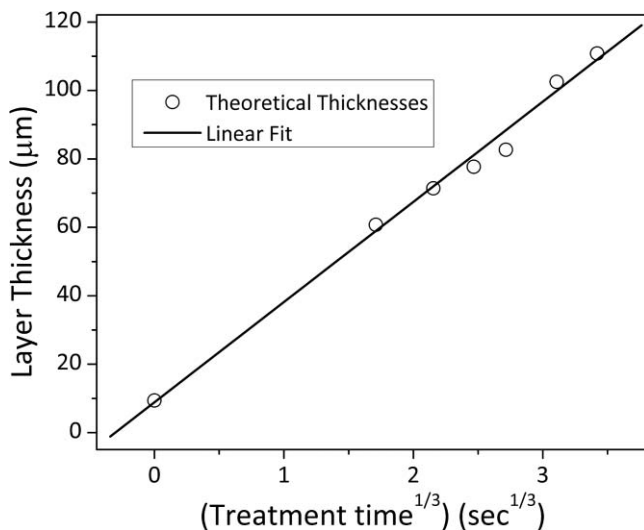


**Fig. 8** Overall lesion depth ( $L_1 + L_2$ ) as a function of demineralization time (days) using thickness values derived from the computational fits. The least-squares best-fit line to the data is  $y(t) = 8.80 + 29.13t^{1/3}$ .

that the considerably different optical and thermal properties of that layer from those of the lesion body contributed sensitively to the overall PTR amplitude and phase frequency response.

In the present investigation, optothermophysical properties of demineralized samples were generated from the theoretical fitting program by first fitting the final demineralized PTR amplitude and phase curve, using thicknesses from TMR analysis as guidelines. Given the PTR amplitude and phase curve fittings and parameters extracted from the untreated state and from the final demineralized state, the thicknesses from the two treatment end points were used to fit PTR experimental data of intermediate measurement points. Prior to discussing the results of the computational fits, it is imperative to emphasize the high fidelity and uniqueness of the fitting procedure for the extraction of optothermophysical parameters from multilayered sound enamel and demineralized lesions. The robustness of the computational algorithm, in addition to evaluation of sources of error in the multiparameter fitting procedure, were also described in Hellen et al.<sup>18</sup>

Optical absorption coefficients for layer 1 increased with demineralization time, while no trend was evident in the absorption properties of the lesion body [Figs. 5(a) and 7(a)]. The higher spatial rate of photon absorption within layer 1 results in the confinement of the subsurface extent of the thermal wave to a narrower region causing a higher amplitude and smaller phase lag.<sup>17</sup> An earlier study that determined optical properties from enamel slabs revealed no evidence of an increase or decrease in optical absorption coefficients between sound and carious enamel; however, large errors (>40%) in the calculated absorption coefficients were observed.<sup>35</sup> Higher scattering coefficients of the developing lesion (layers 1 and 2) are also consistent with the aforementioned PTR trends [Figs. 5(b) and 7(b)]. On demineralization, changes in the scattering coefficient were more dominant than changes in the absorption coefficient, as has been documented.<sup>35</sup> This was caused by crystalline disintegration of the enamel structure and the generation of small pores, which can act as scattering centers.<sup>36,37</sup> Higher scatter of the optical field results in shorter photon path lengths within enamel,<sup>36</sup> which is photothermally tantamount to a higher absorption coefficient (higher photon absorption probability closer to the surface) and increases the generated PTR signal.<sup>15</sup> The previously documented higher reflectance and poorer transmission properties of carious lesions would likely contribute to the localization of the optical field to a narrow region, lessening the influence of the underlying layers.<sup>35,38</sup> The scattering properties of both layer 1 (surface layer) and layer 2 (lesion body) increased substantially from the start of demineralization, with greater scattering contribution from the demineralized lesion body near the end of the treatment period [Figs. 5(b) and 7(b)]. Considering only the first 20 days, a rapid increase in the scattering coefficient of the lesion body from day 0 to day 10 followed a more gradual change from 10 to 20 days [Fig. 7(b)]. Replacement of the demineralizing medium with a fresh aliquot after 20 days most likely dissipated the chemical gradients in the gel surrounding the enamel accelerating the demineralization rate. This may explain the linear increase in scattering coefficient of the lesion body from the 20–40 day period, as well as the concomitant increase in lesion depth over the same period [Fig. 6(b)]. As incipient lesions generate an increasingly inhomogeneous medium, a higher scattering coefficient was expected relative to

sound enamel. Substantial increases in the scattering coefficient of demineralized enamel relative to sound enamel have been documented in the literature. Darling et al.<sup>37</sup> found an increase in the scattering coefficient by one or two orders of magnitude over the scattering coefficient of sound enamel. Spitzer and ten Bosch<sup>35</sup> found a scattering coefficient of white spot lesions to be 5–10 times higher than sound enamel. Higher scattering within the lesion body may occur since this zone occupies the largest volume within the carious lesions, decreasing in mineral volume from 87 vol. % at the sound enamel interface to ~60 vol. % in the subsurface minimum. The enhanced scattering properties of the intact surface layer may be a function of the composite nature of this layer during demineralization. The outer surface layer maintains a level of porosity greater than sound enamel and less than the lesion body (TMR images 3 and 4). Furthermore, the intact surface layer most likely acquired minerals along its inner surface, deposited from the outdiffused flux at the advancing lesion front, as well as outer surface, from mineral deposition from the demineralizing solution at later treatment times, as the buildup of mineral ions in solution increased and the driving force (degree of saturation) for demineralization was reduced. Miake et al.<sup>39</sup> and Tohda et al.<sup>40</sup> showed that demineralized enamel surface layers contained a large number of irregularly shaped crystals of various sizes. The presence of unstructured crystals in the surface layer would augment the scattering properties of layer 1 by creating additional crystal grain boundaries [Figs. 5(b) and 7(b)]. It would also decrease thermal conductivity and diffusivity of the layer, consistently with our findings in layer 1.

Multiparameter fits of PTR experimental data during short and long-term demineralization showed that poorer thermal properties, thermal conductivity and diffusivity, were generated within the lesion body [Figs. 5(c), 5(d), 7(c) and 7(d)]. The creation of microchannels within the demineralized lesion may generate an impedance to heat propagation, resulting in poorer thermal conductivity. A reduction in the thermal conductivity would result in a corresponding reduction in thermal diffusivity based on the direct proportionality between the two quantities. The poorer thermal diffusivity of the lesion body may impede thermal-wave contributions from deeper regions from reaching the enamel surface and as a result confine the region of thermal-wave field within the growing demineralized layer. Investigations on the extraction of thermal properties from carious and sound enamel are scarce. A reduction in the thermal properties of artificially demineralized lesions relative to sound enamel was observed by El-Brolosy et al.<sup>41</sup> using photoacoustic spectroscopy; however, the extent of reduction in conductivity ( $0.72 \text{ W m}^{-1} \text{ K}^{-1}$ ) and diffusivity ( $3.81 \times 10^{-7} \text{ m}^2/\text{s}$ ) values for demineralized enamel were far less than the mean parameter values observed in the present study (Table 1). Intuitively, it might be expected that thermal diffusivity would increase with demineralization due to its inverse relation to density, which decreases within a lesion. However, the increase in lesion porosity results in the filling of the enamel pores with a combination of air and water, both of which have a poorer thermal conductivity,  $0.026$  and  $0.598 \text{ W m}^{-1} \text{ K}^{-1}$ , respectively, than sound enamel ( $\approx 0.87 \text{ W m}^{-1} \text{ K}^{-1}$ ), as well as a higher specific heat capacity.<sup>14,42</sup> This indicates that the balance between the ratio of thermal conductivity to the product of the density and heat capacity will ultimately determine the outcome of the

thermal diffusivity, as well as the fact that residual water within the enamel pores may have a significant influence on thermal diffusion properties of enamel.

Furthermore, the increases in bulk thermal properties, conductivity and diffusivity [Figs. 7(c) and 7(d)] after the 15-day period of demineralization may be indicative of compaction of the demineralized layer ( $L_2$ ) through mineral transport to the enamel surface, with the solid mineral phase having increased conductivity, which ultimately affects the diffusivity. Thus, these contrasting processes in the thermal profiles for the surface and subsurface layer may reflect the dynamic dissolution-reprecipitation processes during lesion formation. A rapid decrease in thermal diffusivity and conductivity of layer 1 for the first 15 days of demineralization was followed by an inversion at later times [Figs. 7(c) and 7(d)]. Initial exposure of enamel to the demineralizing medium likely resulted in superficial mineral loss of the most acid soluble mineral phases. As a result, changes in surface enamel structure would have a significant impact on the optical and thermal energy generation and propagation. The decreasing thermal properties of the surface layer may be related to the superficial removal of mineral phases, which may include the “priming” of the enamel surface<sup>43</sup> and/or etching of the aprismatic layer. A decrease in thickness of layer 1 in the 10-day demineralized sample may support the breakdown of the aprismatic layer toward the formation of the intact surface layer with the concomitant progression of the lesion body inward [Fig. 6(a)]. The initial dissolution of enamel under similar *in vitro* conditions has been shown elsewhere,<sup>44</sup> where a slightly larger surface roughness was induced over a seven-day acid exposure period. An increase in roughness would increase the photothermal signal due to the larger surface-area-to-volume ratio, yielding a higher probability for absorption events and higher thermal-wave fields due to confinement and larger temperature rise at the rough spots. This amounts to effectively poorer thermophysical properties of the surface layer for the first 15 days and effective confinement of optically generated thermal waves within this thermally insulating surface layer, which thus dominates contributions from deeper thermal-wave sources [Figs. 7(c) and 7(d)]. After 15 days, the thermophysical properties of layer 1 increased, which may reflect the well-defined onset of the growing surface layer overlying the lesion body. Similar trends were evident in the subsurface layer, however less pronounced, which may reflect the stabilized thickness of the layer, which may still be experiencing small changes in mineral content. The improved thermal properties of layer 1 may facilitate thermal energy propagation and enhance the interference between forward and  $L_2$  interface-interacted (effectively back propagating) thermal waves. Physically, surface dissolution may dominate earlier demineralization times, generating poorer thermal properties in the surface layer, whereas at later demineralization times, the enhancement of the thermal properties may indicate mineral reprecipitation to restore surface enamel crystallinity. These observations can also account for the minor thermal property improvements in the subsurface lesions. This reaction mechanism is further supported by the changes in thickness of the intact surface layer (layer 1) [Fig. 6(b), inset], which paralleled the change in thermal properties. Little change in the thickness of layer 1 was evident for the first 15 days, whereas substantial mineral gains in the surface layer were found thereafter [Fig. 6(b), inset]. The emergence of a

phase hump (shoulder) at high modulation frequencies ( $>100$  Hz) (Fig. 4) was concomitant with the large increase in the derived thickness for layer 1, which reached a maximum thickness of  $\approx 19$   $\mu\text{m}$ , calculated from the theoretical computational algorithm at the end of the 40-day demineralization period. The phase shoulder at higher modulation frequencies is theoretically explained as the superposition of a second interference pattern generated by the thickening intact surface layer. The absence of the phase shoulder from the 10-day demineralized samples is most likely due to the smaller surface layer thicknesses, which would yield a much smaller interference pattern at much higher frequencies, outside our measurement range (Fig. 3). Growth of the intact surface layer over time was also observed by Gray and Francis,<sup>45</sup> Groeneveld et al.,<sup>20</sup> and Gao et al.<sup>46</sup> in constant volume acid-gel systems. Mineral reprecipitation to increase the thickness of the intact surface layer may be related to the physical properties of the acid-gel medium. Stagnant conditions at the gel-enamel interface and the lack of convection currents in the gel, concentrate mineral ions at the interface, which can effectively reduce the driving forces for demineralization and promote surface mineral reprecipitation at later sample exposure periods. The rapid reduction in thermal conductivity and diffusivity of the lesion body (layer 2) over the first 15 days was followed by relative stability with small increases thereafter [Figs. 7(c) and 7(d)], a behavior that may be explained by the nature of the lesion body during formation. Once passing a particular lesion depth, only minor changes in the minimum mineral volume of the lesion body proceed and rather the lesion body acts as a transport medium for the diffusion of ions to and from the advancing front of the lesion.<sup>47</sup> The slight increase in thermal properties after 15 days may be attributed to mineral deposition throughout the depth of the lesion as dissolved mineral ions are transported from the advancing front toward the enamel surface, as discussed earlier.

Theoretical analysis of PTR amplitude and phase curves allows for the nondestructive evaluation of demineralization kinetics. In the 40-day demineralized sample, a linear rate of lesion growth with the cube root of time was observed (Fig. 8). This relationship between lesion progression and time suggests slower-than-linear one-dimensional diffusion-limited rate ( $\sim t^{1/2}$ ) of enamel demineralization and indicates that multicomponent diffusive transport of acids and/or dissolved mineral ions throughout the depth of the lesion to and from the advancing lesion front is the rate controlling process, as has been documented in earlier reports.<sup>48-51</sup> The linear least-squares fit to the 40-day layer thicknesses revealed that mineral loss progressed at a rate of  $\sim 29$   $\mu\text{m}/\text{s}^{1/3}$  (Fig. 8). At  $t = 0$ , the residual 10- $\mu\text{m}$  layer in Fig. 8 is attributed to the surface aprismatic layer, which was removed during the acid attack toward the formation of the intact surface layer. The onset of a sublinear relationship between lesion width (thickness of layer 2) and demineralization period observed after five days of the 10-day demineralized sample [Fig. 6(a)] is consistent with the subdiffusive trend observed more clearly with the 40-day demineralized sample. Variances in the kinetics due to inter- and intrasample variability as a result of structural and chemical gradients may influence the theoretical extraction of layer thicknesses, particularly with respect to the utilization of natural enamel surfaces and their intrinsically higher fluoride content.<sup>52</sup> Furthermore, this subdiffusive relationship may infer that the rate-controlling process during

demineralization also involves reaction at the crystallite level, as has been documented in earlier studies.<sup>46,47,53</sup> In summary, the variance in lesion progression between the two sample groups further illustrates that the demineralization process is not merely the result of a single mechanism because changes in structural gradients, chemical driving forces, and porosity, among other factors, complicate the process and significantly affect the rate of lesion development. The present evidence using PTR monitoring of demineralization kinetics indicates that dissolution processes *in vitro* entail a continuum of surface and diffusion-controlled mechanisms in agreement with Elliott et al.<sup>54</sup>

#### 4.2 Modulated Luminescence Signal Evolution during Demineralization

The modulated LUM signal channel, which monitors optical radiative processes, produced consistent trends with treatment time. LUM amplitude decreased monotonically and phase decreased at the frequency of the phase minimum ( $\approx 89$  Hz) with demineralization time (Figs. 3 and 4). These trends and the poorer contrast between sound and demineralized enamel are consistent with earlier reports of modulated LUM behavior with respect to artificial demineralized lesions.<sup>11,13</sup> The reduction in LUM with demineralization can fundamentally be explained based on light-scattering and -absorption properties of demineralized enamel with compromised crystallinity leading to decreased optical quantum yields.<sup>34</sup> In addition, alteration of the scattering coefficient in demineralized enamel may have two more effects on the amount of luminescence detected; both scattering of the excitation light before reaching a fluorophore and/or multiple scattering of the converted luminescence light within the tooth before exiting and being collected by the detector, will result in a lower overall fluorescence collection efficiency from demineralized lesions.<sup>55</sup> Opposite to photothermal effects, the higher scattering coefficients of demineralized enamel reduce photon path lengths causing a proportional reduction in the total light path before it emerges at the enamel surface.<sup>36</sup> Additional explanations for the loss of autofluorescent properties have been attributed to the loss of chromophores during the demineralization process and the quenching of fluorescence by a change in the molecular environment of the chromophores.<sup>36,56</sup> Stable and high-SNR normalized LUM phase curves exhibited minima in the midfrequency range characteristic of optical relaxation times determined for enamel.<sup>32</sup> The slight monotonic decrease in phase minima with demineralization may be indicative of the smaller number of excited chromophores, a result of the intense scattering properties and acid-induced apatite crystal collapse, yielding reduced radiative conversion processes (quantum yields) and lower signal amplitude.

LUM has previously shown a strong sensitivity to the degree of de/hydration of the teeth,<sup>13</sup> as has been observed with other optical detection modalities such as QLF,<sup>22</sup> and may be imbedded within the monotonicity of the LUM trends with demineralization and difficult to uncouple from actual changes in mineralization. It is also important to highlight the anticorrelation between trends in LUM amplitude and phase and those of PTR, where the largest increase in PTR amplitude yielded the largest decrease in LUM amplitude. This effect can be explained based on the abovementioned light scattering properties and also on the photophysical versus photothermal processes in the

trade-off between radiative and nonradiative energy-conversion efficiency, respectively. In terms of the thermal-wave signal, enhanced light-scattering coefficients would confine the thermal centroid<sup>15</sup> closer to the enamel surface, yielding a higher amplitude and smaller phase lag. In contrast, in terms of LUM, the higher optical scattering coefficients will result in higher fluence due to energy confinement over a smaller sample depth. However, crystalline destruction during demineralization will enhance the nonradiative component as excited chromophores lose their radiative energy conversion pathways and channel the absorbed energy into nonradiative (thermal) emissions. Thus, the outcome of a reduced radiative component and increased nonradiative component is a smaller LUM signal and larger PTR signal, respectively. This illustrates the complementary nature of the generated PTR and LUM signals.

## 5 Summary and Conclusions

As a nondestructive technique, the combination of PTR and LUM provides four distinct signal channels along with a comprehensive theoretical and computational formalism to yield quantitative information regarding the evolution of enamel demineralization in terms of lesion severity and its change over time. Although the results of the present study cannot be directly extrapolated to clinical environments, they undoubtedly advance the discipline of quantitative dental diagnostics and form the widest parameter basis for future research in the field. Furthermore, given the high fidelity and uniqueness of fit of the multiparameter estimation of enamel lesion properties,<sup>18</sup> the computational algorithm employed in the present study may be a valuable tool for noninvasive quantification of enamel caries and possibly nondestructively selecting uniform lesions for remineralization studies, because the parameters of a demineralized lesion can have a marked impact on the outcome of subsequent remineralization.<sup>57</sup> Quantitative extraction of optical and thermal properties from intact, whole teeth, rather than prepared thin sections, allows for the investigation of optothermophysical parameters under conditions more relevant to the natural intraoral environment. The promising results from the present investigation place the quantitative PTR and LUM technique at an advantage for nondestructive caries evaluation *in vitro* over conventional purely optical methods, in terms of the total information extracted from the generated signals by virtue of depth profilometry. The present study illustrates the first account where demineralized enamel could be resolved into three effective layers, where the nondestructive extraction of optothermophysical parameters of each layer allowed for depth-profile reconstructions of these parameters in enamel as a function of treatment time. In light of the results of the present study, PTR-LUM proved to be efficacious in detecting and quantifying mineralized layers generated during demineralization processes and holds promise for future applications as a clinical evaluation tool, although further testing and refinements are necessary.

### Acknowledgments

A.M. acknowledges funding from the Ministry of Research and Innovation, the Ontario Premier's Discovery Award, the Canadian Foundation for Innovation & Ontario Research Fund, and the Canada Research Chairs Program, as well as the Natural

Sciences and Engineering Research Council of Canada for a Discovery Grant. The authors also acknowledge Dr. Stephen Abrams of Quantum Dental Technologies for his input and valuable discussions.

## References

- J. J. M. Damen, R. A. M. Exterkate, and J. M. ten Cate, "Reproducibility of TMR for the determination of longitudinal mineral changes in dental hard tissues," *Adv. Dent. Res.* **11**, 415–419 (1997).
- O. Minet, K. Dörschel, and G. Muller, "Lasers in biology and medicine," *Laser Appl. Landolt-Börnstein* **8**, 279–310 (2006).
- C. Robinson, R. C. Shore, S. J. Brookes, S. Strafford, S. R. Wood, and J. Kirkham, "The chemistry of enamel caries," *Crit. Rev. Oral Biol. Med.* **11**(4), 481–495 (2000).
- D. Spitzer and J. J. ten Bosch, "The absorption and scattering of light in bovine and human dental enamel," *Calcif. Tissue Res.* **17**, 129–137 (1975).
- D. Fried, R. E. Glena, J. D. B. Featherstone, and W. Seka, "Nature of light scattering in dental enamel and dentin at visible and near-infrared wavelengths," *Appl. Opt.* **34**, 1278–1285 (1995).
- M. Braden, "Heat conduction in normal human teeth," *Arch. Oral Biol.* **9**, 479–486 (1964).
- W. S. Brown, W. A. Dewey, and H. R. Jacob, "Thermal properties of teeth," *J. Dent. Res.* **49**, 752–755 (1970).
- M. Saitoh, Y. Shiota, K. Kaneko, J. Hayashi, H. Moro, H. Koizumi, T. Igarashi, and M. Nishiyama, "Thermal properties of dental materials: part 10 crown and bridge resins containing high concentration of filler," *Jpn. J. Dent. Mater.* **19**, 441–447 (2000).
- A. J. Panas, M. Preiskorn, M. Dabrowski, and S. Žmuda, "Validation of hard tooth tissue thermal diffusivity measurements applying an infrared camera," *Infrared Phys. Technol.* **49**(3), 302–305 (2007).
- R. J. Jeon, C. Han, A. Mandelis, V. Sanchez, and S. H. Abrams, "Diagnosis of pit and fissure caries using frequency-domain infrared photothermal radiometry and modulated laser luminescence," *Caries Res.* **38**, 497–513 (2004).
- R. J. Jeon, A. Mandelis, V. Sanchez, and S. H. Abrams, "Non-intrusive, non-contacting frequency-domain photothermal radiometry and luminescence depth profilometry of natural carious and artificial sub-surface lesions in human teeth," *J. Biomed. Opt.* **9**, 804–819 (2004).
- R. J. Jeon, A. Matvienko, A. Mandelis, S. H. Abrams, B. T. Amaechi, and G. Kulkarni, "Detection of interproximal demineralized lesions on human teeth in vitro using frequency-domain infrared photothermal radiometry and modulated luminescence," *J. Biomed. Opt.* **12**, 034028 (2007).
- R. J. Jeon, A. Hellen, A. Matvienko, A. Mandelis, S. H. Abrams and B. T. Amaechi, "In vitro detection and quantification of enamel and root caries using infrared photothermal radiometry and modulated luminescence," *J. Biomed. Opt.* **13**, 034025 (2008).
- D. Almond and P. Patel, *Photothermal Science and Techniques*, Kluwer Academic Publishers, Chapman and Hall, London (1996).
- A. Mandelis, *Diffusion Wave Fields: Mathematical Methods and Green Functions*, Springer, New York (2001).
- A. Matvienko, A. Mandelis, and S. H. Abrams, "Robust multiparameter method of evaluating the optical and thermal properties of a layered tissue structure using photothermal radiometry," *Appl. Opt.* **48**, 3193–3204 (2009).
- A. Matvienko, A. Mandelis, A. Hellen, R. J. Jeon, S. H. Abrams, and B. T. Amaechi, "Quantitative analysis of incipient mineral loss in hard tissues," *Proc. SPIE* **7166**, 71660C (2009).
- A. Hellen, A. Matvienko, A. Mandelis, Y. Finer, and B. T. Amaechi, "Opto-thermophysical properties of demineralized human dental enamel determined using photothermally generated diffuse photon density and thermal wave fields," *Appl. Opt.* **49**(36), 6938–6951 (2010).
- J. Arends and J. Schuthof, "Microhardness and lesion depth studies of artificial caries lesions: a comparison of gelatin and HEC based systems," *J. Biol. Buccale* **8**(2), 175–81 (1980).
- A. Groeneveld, D. J. Purdell-Lewis, and J. Arends, "Influence of the mineral content of enamel on caries-like lesions produced in hydroxyethylcellulose buffer solutions," *Caries Res.* **9**, 127–138 (1975).
- B. T. Amaechi, S. M. Higham, and W. M. Edgar, "Factors affecting the development of carious lesions in bovine teeth *in vitro*," *Arch. Oral Biol.* **43**, 619–628 (1998).
- S. Al-Khateeb, R. A. M. Exterkate, E. de Josselin de Jong, B. Angmar-Månsson, and J. M. ten Cate, "Light-induced fluorescence studies on dehydration of incipient enamel lesions," *Caries Res.* **36**, 25–30 (2002).
- R. Gmur, E. Giertsen, M. H. Van Der Veen, E. de Josselin de Jong, J. M. ten Cate, and B. Guggenheim, "In vitro quantitative light-induced fluorescence to measure changes in enamel mineralization," *Clin. Oral Invest.* **10**, 187–195 (2006).
- I. A. Pretty, W. M. Edgar, and S. M. Higham, "Detection of *in vitro* demineralization of primary teeth using quantitative light-induced fluorescence (QLF)," *Int. J. Paediatr. Dent.* **12**, 158–167 (2002).
- X. Z. Zhang, P. Anderson, S. E. P. Dowker, and J. C. Elliott, "Optical profilometric study of changes in surface roughness of enamel during *in vitro* demineralization," *Caries Res.* **34**, 164–174 (2000).
- E. de Josselin de Jong, A. H. I. M. Linden, and J. J. ten Bosch, "Longitudinal microradiography: a non-destructive automated quantitative method to follow mineral changes in mineralised tissue slices," *Phys. Med. Biol.* **32**, 1209–1220 (1987).
- W. H. Press, B. P. Flannery, S. A. Teukolsky, and W. T. Vetterling, *Numerical Recipes in C*, Cambridge University Press, Cambridge, England (1988).
- A. Matvienko, A. Mandelis, R. J. Jeon, and S. H. Abrams, "Theoretical analysis of coupled diffuse-photon-density and thermal-wave field depth profiles photothermally generated in layered turbid dental structures," *J. App. Phys.* **105**, 102022 (2009).
- L. W. Ripa, A. J. Gwinnett, and M. G. Buonocore, "The 'prismless' outer layer of deciduous and permanent enamel," *Arch. Oral Biol.* **11**, 41–48 (1966).
- A. J. Gwinnett, "The ultrastructure of the 'prismless' enamel of permanent human teeth," *Arch. Oral Biol.* **12**, 381–387 (1967).
- T. Kodaka, "Scanning electron microscopic observations of surface prismless enamel formed by minute crystals in some human permanent teeth," *Anat. Sci. Int.* **78**(2), 79–84 (2003).
- L. Nicolaides, A. Mandelis, and S. H. Abrams, "Novel dental dynamic depth profilometric imaging using simultaneous frequency-domain infrared photothermal radiometry and laser luminescence," *J. Biomed. Opt.* **5**, 31–39 (2000).
- C. A. Bennett, Jr., and R. R. Patty, "Thermal wave interferometry: a potential application of the photoacoustic effect," *Appl. Opt.* **21**, 49–54 (1982).
- C. Mujat, M. H. van der Veen, J. L. Ruben, J. J. ten Bosch, and A. Dogariu, "Optical pathlength spectroscopy of incipient caries lesions in relation to quantitative light fluorescence and lesion characteristics," *Appl. Opt.* **42**, 2979–2986 (2003).
- D. Spitzer and J. J. ten Bosch, "Luminescence quantum yields of sound and carious dental enamel," *Calcif. Tissue Res.* **24**, 249–251 (1977).
- B. Angmar-Månsson and J. J. ten Bosch, "Optical methods for the detection and quantification of caries," *Adv. Dent. Res.* **1**, 14–20 (1987).
- C. Darling, G. Huynh, and D. Fried, "Light scattering properties of natural and artificially demineralized dental enamel at 1310-nm," *J. Biomed. Opt.* **11**, 034023 (2006).
- C. C. Ko, D. Tantbirojn, T. Wang, and W. H. Douglas, "Optical scattering power for characterisation of mineral loss," *J. Dent. Res.* **79**, 1584–1589 (2000).
- Y. Miate, Y. Saeki, M. Takahashi, and T. Yanagisawa, "Remineralization effects of xylitol on demineralized enamel," *J. Electron Microsc.* **52**, 471–476 (2003).
- H. Tohda, T. Yanagisawa, N. Tanaka, and S. Takuma, "Growth and fusion of apatite crystals in the remineralized enamel," *J. Electron Microsc.* **39**, 238–244 (1990).
- T. A. El-Brolossy, S. Abdalla, O. E. Hassanein, S. Negm, and H. Talaat, "Photoacoustic and electron microscopic studies of remineralized artificially carious enamel and dentin," *J. Phys. IV* **125**, 685–688 (2005).
- N. B. Vargaftik, L. P. Filippov, A. A. Tarzimanov, and E. E. Totskii, *Handbook of Thermal Conductivity of Liquids and Gases*, pp. 68–70, CRC Press, Boca Raton (1994).

43. E. C. Moreno and R. T. Zahradnik, "Chemistry of enamel subsurface demineralization *in vitro*," *J. Dent. Res.* **53**(Suppl. 2), 226–235 (1974).
44. R. A. J. Groenhuis, W. L. Jongebloed, and J. J. ten Bosch, "Surface roughness measurement of acid-etched and demineralized bovine enamel measured by a laser speckle method," *Caries Res.* **14**, 333–340 (1980).
45. J. A. Gray and M. D. Francis, "Physical chemistry of enamel dissolution," in *Mechanisms of Hard Tissue Destruction*, R. F. Sognaes, Ed., pp. 213–260, Publ. Am. Assoc. Adv. Sci. Washington, DC (1963).
46. X. J. Gao, J. C. Elliott, and P. Anderson, "Scanning microradiographic study of the kinetics of subsurface demineralization in tooth sections under constant-composition and small constant-volume conditions," *J. Dent. Res.* **72**, 923–930 (1993).
47. J. Arends, J. L. Ruben, and D. Inaba, "Major topics in quantitative microradiography of enamel and dentin: R parameter, mineral distribution visualization, and hyper-remineralization," *Adv. Dent. Res.* **11**, 403–414 (1997).
48. W. I. Higuchi, J. A. Gray, J. J. Hefferren, and P. R. Patel, "Mechanisms of enamel dissolution in acid buffers," *J. Dent. Res.* **44**, 330–341 (1965).
49. D. F. G. Poole, R. P. Shellis, and J. E. Tyler, "Rates of formation *in vitro* of dental caries-like enamel lesions in man and some non-human primates," *Arch. Oral Biol.* **26**, 413–417 (1981).
50. J. D. B. Featherstone, J. F. Duncan, and T. W. Cutress, "A mechanism for dental caries based on chemical processes and diffusion phenomena during *in vitro* caries simulation on human tooth enamel," *Arch. Oral Biol.* **24**, 101–112 (1979).
51. J. D. B. Featherstone and J. R. Mellberg, "Relative rates of progress of artificial carious lesions in bovine, ovine and human enamel," *Caries Res.* **15**, 109–114 (1981).
52. J. Weatherell, C. Robinson, and A. S. Hallsworth, "Variation in the chemical composition of human enamel," *J. Dent. Res.* **53**, 180–192 (1974).
53. P. Anderson, F. R. G. Bollet-Quivogne, S. E. P. Dowker, and J. C. Elliott, "Demineralization in enamel and hydroxyapatite aggregates at increasing ionic strengths," *Arch. Oral Biol.* **49**, 199–207 (2004).
54. J. C. Elliott, S. E. P. Dowker, G. R. Davis, C. S. Walker, H. S. Wassif, and P. Anderson, "Is the rate of demineralisation in a caries lesion diffusion or surface reaction controlled?" *Caries Res.* **42**, 203–204 (2008).
55. J. M. Girkin, A. F. Hall, and S. L. Creanor, "Multi-photon imaging of intact dental tissue," in *Proc. of 4<sup>th</sup> Annual Indiana Conf. on Early Detection of Dental Caries II*, G. K. Stookey, ed. pp. 155–168, Indiana University School of Dentistry, Indianapolis (2000).
56. U. Hafstrom-Bjorkman, F. Sundstrom, E. de Josselin de Jong, A. Oliveby, and B. Angmar-Mansson, "Comparison of laser fluorescence and longitudinal microradiography for quantitative assessment of *in vitro* enamel caries," *Caries Res.* **26**, 241–247 (1992).
57. R. J. M. Lynch, U. Mony, and J. M. ten Cate, "Effect of lesion characteristics and mineralizing solution type on enamel remineralization *in vitro*," *Caries Res.* **41**, 257–262 (2007).